BISTROP: Bayesian Inversion of SpecTral levels RatiOs and P wave polarities for focal mechanism determination

Authors

Raffaella De Matteis[1], Vincenzo Convertito[2] and Aldo Zollo[3]

Affiliations

[1]*Dipartimento di Scienze e Tecnologie, Università del Sannio*

Via dei Mulini, 59/A, 82100 Benevento, Italy

[2]*Istituto Nazionale di Geofisica e Vulcanologia – Osservatorio Vesuviano*

Via Diocleaziano, 328, 80145 Napoli, Italy

[3]*Dipartimento di Fisica, Università Federico II di Napoli*

Complesso universitario di Monte S.Angelo, via Cinthia, 80124 Napoli, Italy

Correspondig author

De Matteis Raffaella

Università del Sannio, Dipartimento di Scienze e Tecnologie

Via dei Mulini, 59/A, 82100 Benevento, Italy

Email: raffaella.dematteis @unisannio.it

Abstract

The analysis of earthquakes focal mechanism provides information about the stress regime, fault geometry and deformation processes acting in a given region. Generally, the techniques aimed at determining focal mechanism are designed to work in specific magnitude range operating both in the time and frequency domain, and using different data (e.g., P-polarities, S-wave polarization, S/P amplitude ratios, etc.). In this paper we present a new method named BISTROP that can be applied to both small and moderate-to-large magnitude events. BISTROP uses a Bayesian approach to jointly invert the long-period spectral level P/S ratios and the P-polarities to infer the fault plane solutions. We apply this method to analyze synthetic data as well as those generated by real earthquakes. We find that the obtained solutions for moderate earthquakes are comparable with those obtained by using moment tensor inversion, and they are more constrained with respect to the solutions obtained using only P-polarity data for small earthquakes.

Introduction

A thorough understanding of earthquake focal mechanisms gives information about the stress regime that originates the occurrence of the earthquakes and their relation to the regional tectonics. The currently available techniques for the focal mechanism estimation are designed to work on specific magnitude ranges. In particular, for moderate-to-large earthquakes waveforms or spectral data inversions is performed to yield stable solutions (Dreger and Helmberger, 1993; Dreger, 2003; Delouis, 2014; Fojtíková and Zahradnik, 2014). The same approach cannot be easily applied to small earthquakes due to the higher noise level and to the generally inadequate description of the medium response at the wavelengths at which micro-earthquakes radiate. However, source characterization of small earthquakes can be a useful tool to obtain information on the seismogenic structures, the stress field and its variations in time and space. This is of particular relevance in those areas where seismicity rate is low due to long inter-seismic periods or in areas where seismicity is induced by man-made activities. In addition, in many seismic regions worldwide current seismic networks are densely spaced and equipped with high dynamic sensors and data loggers. This has significantly decreased the minimum detectable magnitude and has greatly increased the number of recordings for small earthquakes. As a consequence, it is necessary that the techniques can be used for a massive data analysis, reaching the limit of the real-time analysis.

The determination of the focal mechanism for small earthquakes is hampered by several factors. For example, moment tensor inversion, that is the more stable and robust technique for moderate-to-large earthquakes analysis, may not be suitable for small earthquakes, since it requires a precision on source location, and details about the propagation medium (Green's function) at a scale that is rarely achievable. Moreover, the number of stations that record small events reduces with distance from the source making inefficient, for example, the application of methods based on the use of the P-wave polarities. Also the techniques that use P- and S-waves amplitudes cannot be easily used because, being the recorded signal richer in high-frequencies, it is contaminated by wave diffraction at small-scale crustal heterogeneities. In a recent study, Fojtíková and Zahradnik (2014) have proposed a method called CSPS (Cyclic scanning of the Polarity Solutions), aimed at reducing the uncertainty of the solutions obtained by methods based on the inversion of the P-wave polarities. For a given distribution of observed P-wave polarities, the solutions obtained by means of the inversion code inversion FOCMEC (Snoke, 2003), one by one are used as input to the inversion of the waveform at a single station. The best model will be the one characterized by the minimum variance. Since this method uses a single station the solution might strictly depend on the quality of the input waveform.

Several studies have proposed the use of the S/P amplitudes ratio including Kisslinger (1980), Kisslinger et al. (1981), Julian and Foulger (1996), Rau et al. (1996) and Shen et al. (1997) and more recently Hardebeck and Shearer

(2003). These latter authors have used the S/P amplitudes ratio in addition to polarities, to better constrain the focal mechanism of earthquakes with magnitude lower than 4. The S/P ratio enables to neglect the magnitude and the geometrical attenuation, and to consider only site effects and the difference between the P-waves and S-waves anelastic attenuation.

A stable and robust alternative is the joint use of P-polarities and S-wave polarization, which are less affected by propagation effects compared to the amplitudes. In this respect, Zollo et al. (1991) have proposed a non-linear inversion method for studying the earthquake mechanism by computing the posterior probability of parameters (strike, dip and slip fault angles) for the given observational data sets by using a Bayesian approach. The method allows to locate the maximum likelihood solutions, and to get a reliable estimate of the parameter correlation and resolution. Subsequently, several authors have applied the same or a similar technique to a variety of earthquake studies (e.g., Iannaccone et al., 1994; Walsh et al., 2009). However, the method relies on the capability to precisely measure the S-wave polarization, which can be a difficult task in case of noisy records or in presence of dominant multi-path and anisotropy effects. Recently, Imanishi et al. (2016), have proposed a technique for focal mechanism determination of nonvolcanic tremor using S-wave polarization after removing anisotropy effects.

Zahradnik et al. (2001) have proposed an inversion method to determine the focal mechanism of small earthquakes (M 3.4–3.7), called ASPO (Amplitude Spectra and Polarities) that operates in the frequency domain.

126 The method is based on the comparison between the amplitude spectrum of
127 the whole recorded signal and the one calculated from synthetic
128 seismograms for different sets of strike, dip and rake, and for different
129 values of the scalar seismic moment and hypocenter. The polarities are used
130 in the final step to accept or reject the obtained solution. As for most of
131 other methods, the performance of this technique depends on the level of
132 knowledge about the propagation medium and the capability to simulate the
133 high frequency spectral content of real earthquakes.

134 In the present study we propose a method for estimating the focal
135 mechanism of earthquakes modeled as a double couple (DC) point source
136 shear-dislocation able to work with both moderate-to-large and small
137 events. The technique, named BITROP, which stands for Bayesian
138 Inversion of SpecTral levels RatiOs and P-wave polarities, jointly inverts
139 the ratio between P- and S-wave long-period spectral levels and the P-wave
140 polarities in a Bayesian framework. Concerning the input data, spectral
141 levels are easier to be measured compared to other observables (e.g., S-
142 wave polarization or P- and S-waves amplitudes) and, as a consequence,
143 they are generally available for a broad range of magnitude. Formally, the
144 method is based on the relationship between the theoretical radiation pattern
145 and the long-period spectral level calculated from the first P- or S-waves at
146 different stations. Unlike inversion methods that use only the polarity of the
147 first arrivals, whose identification is not always easy because of the
148 background noise, BISTROP does not impose the need to identify the first
149 arrival with the same precision; it will be sufficient that the portion of the

150 seismogram used for the spectral inversion contains the selected first arrival
151 and does not include other seismic phases. However this does not exclude
152 the need of few P-polarities to better constrain the mechanism. Moreover,
153 working with the ratio between low-frequency part of the P- and S-wave
154 spectra allows to reduce, in first approximation, if they are not known, the
155 effects of the geological soil condition (site effect) and of both geometric
156 and anelastic attenuation. Note that, the probabilistic formulation of the
157 inverse problem allows obtaining a thorough description of the inferred
158 parameters (i.e., uncertainty and correlation).

159 As example of application to a moderate event, we analyzed the 23
160 December 2013, M_W 5.0, Matese, Italy, earthquake. This event has been
161 recorded by a high number of stations of different seismic networks with a
162 good azimuthal coverage and its focal mechanism has been accurately
163 obtained from moment tensor inversion.

164 Regarding the small magnitude earthquakes, optimal conditions in terms of
165 station distribution and signal-to-noise ratio are less frequently verified. As
166 a consequence, we first set up a synthetic test on a simulated M_L 2.9
167 earthquake recorded at a network reproducing the geometry of the Irpinia
168 Seismic Network (ISNet) (Weber et al., 2007). Next we applied it to two
169 different earthquakes occurred in Southern Italy and characterized by
170 different focal mechanisms and recorded at seismic networks with different
171 azimuthal coverage: the 27 May 2009, M_L 2.9, Laviano earthquake and the
172 27 September 2012, M_L 4.1, Benevento earthquake.

Method

Seismic moment can be measured from the far-field P-wave displacement spectra using the relation (Aki and Richards, 1980):

$$M_0 = \frac{4\pi\rho_s^{1/2}\rho_r^{1/2}\alpha_s^{5/2}\alpha_r^{1/2}R'\Omega_0^P}{F\langle|\mathcal{R}_{\theta\varphi}^P|\rangle} \quad (1)$$

where ρ_s and ρ_r are the medium densities at the source and at the receiver, respectively; α_s and α_r are the P-wave velocities at the source and at the receiver, respectively; F is the free-surface effect; Ω_0^P is the long-period spectral level of the P-wave and $\langle\mathcal{R}_{\theta\varphi}^P\rangle$ is the average P-wave radiation pattern; R' is the geometrical spreading estimated for a linear variation of velocity with depth (Ben-Menahem and Singh, 1981):

$$R' = \sqrt{\frac{\rho_r\alpha_r}{\rho_s\alpha_s}}\frac{R}{sini_h} \quad (2)$$

where R is the epicentral distance and i_h is the take-off angle.

Equivalently, for the S-wave it is possible to write a similar expression,

$$M_0 = \frac{4\pi\rho_s^{1/2}\rho_r^{1/2}\beta_s^{5/2}\beta_r^{1/2}R'\Omega_0^S}{F\langle|\mathcal{R}_{\theta\varphi}^S|\rangle} \quad (3)$$

where β is the S-wave velocity (at the source β_S and at the receiver β_r, respectively), Ω_0^S is the long-period spectral level of the S-wave and $\langle\mathcal{R}_{\theta\varphi}^S\rangle$

191 is the S-wave average radiation pattern. The formulation for the geometrical
192 spreading R' is as reported in eq. (2) but using the β values.
193 The long-period spectral level can be measured from the observed
194 displacement spectrum assuming a given source and attenuation model.
195 According to Boatwright (1980), the displacement source spectrum can be
196 described as:
197

$$S(f) = \frac{\Omega_o}{\left[1 + \left(\frac{f}{f_c}\right)^{\zeta n}\right]^{1/n}} \qquad (4)$$

198 where f is the frequency, f_c the corner frequency, ζ the high-frequency fall
199 off rate, and n is a constant. As for the attenuation, we assumed the
200 exponential decay filter:
201

$$Q(f) = e^{-\pi f \frac{T}{Q_f}} \qquad (5)$$

202
203 where T is the travel-time, Q_f has a general formulation given by $Q_f = Q_o f^n$
204 where Q_o is the quality factor evaluated at the reference frequency of 1Hz
205 (Morozov, 2008). In the present study we assumed n=0, that is, a frequency
206 independent quality factor.
207 Equations (1) and (3) assume an average radiation pattern coefficient 0.52
208 and 0.63 for P- and S-wave, respectively (Aki and Richards, 1980).
209 Actually, for a double-couple source model, the radiation pattern depends
210 on the fault orientation, through the angles strike ϕ and dip δ, on the rake
211 angle λ, and on the take-off angle i_h (Aki and Richards, 1980). Thus, for a

given earthquake, if the focal mechanism and the source-station relative position are known, the functions $\mathcal{R}^P = \mathcal{R}^P(\phi, \delta, \lambda, i_h, \phi_R)$ and $\mathcal{R}^S = \mathcal{R}^S(\phi, \delta, \lambda, i_h, \phi_R)$, being ϕ_R the source-receiver azimuth, can be substituted in equations (1) and (3). Using the new formulation for eq.(1) and eq.(3), , it results that:

$$\frac{\mathcal{R}^P(\phi, \delta, \lambda, i_h, \phi_R)}{\mathcal{R}^S(\phi, \delta, \lambda, i_h, \phi_R)} = \left(\frac{\alpha_s^2 \alpha_r}{\beta_s^2 \beta_r}\right) \frac{\Omega_0^P}{\Omega_0^S} \qquad (6)$$

For a given earthquake that has been located by using *N* recording stations and a specific velocity model the variables i_h and ϕ_R, as well as the α and β are known quantities. Thus, at least in principle, if it is possible to accurately measure the long-period spectral levels, the ratio Ω_0^P/Ω_0^S plotted as a function of the source-receiver azimuth would match the ratio between the radiation pattern coefficients.

The aim of the present study is to jointly invert the observed Ω_0^P/Ω_0^S ratios along with the observed P-wave polarities, to infer the focal mechanism parameters (ϕ, δ, λ), by using a Bayesian framework. The approach is similar to that proposed by Zollo and Bernard (1991) but uses different proxies. Specifically, given the vector of model parameters $\boldsymbol{m}$ whose components are the angles (ϕ, δ, λ), and a vector of observed data $\boldsymbol{d}$, we aim at inferring an *a-posteriori* probability density function $q(\boldsymbol{m}|\boldsymbol{d})$ given by:

$$q(\boldsymbol{m}|\boldsymbol{d}) = \frac{f(\boldsymbol{d}|\boldsymbol{m})p(\boldsymbol{m})}{\int_M f(\boldsymbol{d}|\boldsymbol{m}')p(\boldsymbol{m}')\, d\boldsymbol{m}'} \qquad (7)$$

where $f(\boldsymbol{d}|\boldsymbol{m})$ is the conditional probability function that represents the probability density function (pdf) associated with possible data realizations for a fixed parameter vector $\boldsymbol{m}$ in the model parameter space $\boldsymbol{M}$, and $p(\boldsymbol{m})$ is the *a-priori* pdf. In the present study the data vector $\mathbf{d}$ is composed by N_L measurements of Ω_0^P/Ω_0^S ratios ($\mathbf{d}^L$) and N_P measurements of P polarities ($\mathbf{d}^P$). As a consequence, given that P-wave polarities and spectral ratios are independent data sets, the conditional probability function may be written as $f(\mathbf{d}|\mathbf{m})=f(\mathbf{d}^L|\mathbf{m})f(\mathbf{d}^P|\mathbf{m})$.

Assuming that the N_L Ω_0^P/Ω_0^S observations are independent and normally distributed, the $f(\boldsymbol{d}^L|\boldsymbol{m})$ can be formulated as

$$f(\boldsymbol{d}^{\boldsymbol{L}}|\boldsymbol{m}) = f\left(d_1, \dots, d_{N_L}\middle|\boldsymbol{m}\right) = \prod_{i=1}^{N_L} \frac{1}{\sqrt{2\pi}\sigma_i} \exp\left(-\frac{\{d_i - [G(\boldsymbol{m})]_i\}^2}{2\sigma_i^2}\right) \qquad (8)$$

where $G(\boldsymbol{m})$ represents a functional relationship between models and data and corresponds to equation 6. Assuming homoscedasticity for the analyzed variables (that is the observables have the same finite variance) eq.(8) is written as:

$$f(\boldsymbol{d}^L|\boldsymbol{m}) = \frac{1}{\left(\sqrt{2\pi}\sigma\ \right)^{N_L}} exp\left(-\frac{\sum_{i=1}^{N_L}\{d_i - [G(\boldsymbol{m})]_i\}^2}{2\sigma^2}\right) \qquad (9)$$

The σ value is estimated from the uncertainty on spectral measure and the term in the summation for the *i*-th observation is

$$w_i \left[\left(\frac{\mathcal{R}^P}{\mathcal{R}^S} \right)_i^{Obs} - \left(\frac{\mathcal{R}^P}{\mathcal{R}^S} \right)_i^{Theo} \right]^2 \qquad (10)$$

The coefficient w_i is a weighting factor that depends on the take-off angle value. In practice, one can decide to give less weight to data observed at stations for which the i_h values are close to 90°.

As regard $f(\mathbf{d}^P|\mathbf{m})$ we use the formulation proposed by Brillinger et al. (1980):

$$f(\boldsymbol{d}^P|\boldsymbol{m}) = \prod_{i=1}^{N_P} \frac{1}{2}[1 + \psi(\mathcal{R}_i^P, \gamma_i, \rho_0) Y_i sign(\mathcal{R}_i^P)] \qquad (11)$$

where $\psi(\mathcal{R}_i^P, \gamma_i, \rho_0) = (1 - 2\gamma_i)\text{erf}(|\rho_0 \mathcal{R}_i^P(\boldsymbol{m})|)$ and erf(*) is the error function.

The quantity in square brackets in eq.(11) gives the probability that the observed *i*th polarity Y_i is coherent with the one computed from the model $\boldsymbol{m}$. $\mathcal{R}_i^P$ is the theoretical $\boldsymbol{P}$ amplitude at station i for a given fault and $sign(\mathcal{R}_i^P)$ is its polarity. The parameters ρ_0 and γ control the shape of the pdf and range between [0,∞) and [0,1/2], respectively. They take into account for the errors in ray tracing (and medium velocity) and the uncertainty on polarity reading. For imprecise polarity data γ is near 0.5 or ρ_0 near 0; precise data correspond to small γ and large ρ_0 (ρ_0 >20). The formulation of the pdf proposed by Brillinger (1980) has the property that the larger the magnitude of $\mathcal{R}_i^P$, the higher is the probability of measuring the correct polarity.

The pdf $p(\boldsymbol{m})$ represents the *a-priori* probability associated with a given model parameter in the model parameter space *M*. The selection of a proper $p(\boldsymbol{m})$ is crucial and must enclose all the available information about the models before gathering the data. In the method implemented in the present study, it is possible to select both a *null informative* probability, which corresponds to a uniform pdf on *M* or a tridimensional Gaussian pdf centered on a given point of *M* with a prescribed degree of correlation among the parameters. The latter formulation could be used for example to restrict the explored mode space when, according to the stress-regime of a given area, some focal mechanisms are more likely than others.

For each analyzed event, the best model $\boldsymbol{m_b}$ corresponds to the maximum a posteriori (MAP) model of the *a-posteriori* pdf (Aster et al., 2013). A mere graphical representation of the pdf as a function of the model parameters can provide global information about the solution quality, highlighting for example the presence of secondary maxima and the possible correlation among the parameters. However, the availability of the *a-posteriori* pdf allows to quantitatively evaluate the uncertainty level associated to the MAP model. Since a Bayesian approach is used, the 68%, 90% and 95% "Bayesian confidence intervals" or simply "confidence intervals" are computed (Carlin and Louis, 2009). By definition a 100x(1-α)% credible set for $\boldsymbol{m}$ is a subset *C* of the space model parameters such that:

$$1 - \alpha \leq \int_C q(\boldsymbol{m}|\boldsymbol{d}) d\boldsymbol{m}$$

where α is the significance level. In addition, the posterior marginal PDFs on each component of $\boldsymbol{m}$ are computed by integrating the $q(\boldsymbol{m}|\boldsymbol{d})$ on the remaining nuisance components.

Data analysis

In the present study we analyzed recordings of velocimeters and/or accelerometers of three different networks that are ISNet, Rete Accelerometrica Nazionale (RAN) managed by the Italian Civil Protection Department and Italian Seismic Network managed by Istituto Nazionale di Geofisica e Vucanologia (INGV). In order to compute the displacement spectra, we have manually windowed all the available waveforms by considering a different duration for P- and S-wave. The selected P window includes at least 0.5 s of pre-P signal and the whole P-wave train. For the S window, the pre-S signal is shorter to avoid possible overlap with the P-wave train, and contains the whole S-wave train. Figure 1 shows an example of the selected P and S windows on the waveforms recorded at LIO3 station (Figure 2a) during the M_L 2.9, Laviano earthquake, together with the observed displacement spectra, the fitting curves and the spectrum of pre-P noise. We tested the sensitivity of the retrieved focal mechanism to the window length and verified that the results are almost insensitive to a variation up to ~30% of the initial window length. Figures 1b and 1c show the comparison between displacement spectra computed on the initial selected time window (Fig. 1a) and those computed by a reduction of 30%

313 of the window length for P- and S-wave, respectively. Examples for other
314 stations are shown in Figures S1 and S2, available in the electronic
315 supplement to this article.
316 Each windowed time series is then tapered by using a 5% cosine taper
317 function and zero padded before computing the Fourier amplitude spectra.
318 The spectra have been converted to displacement spectra (through a single
319 or double integration in the frequency domain) and smoothed by applying
320 an average moving window with a two-point half width.
321 We considered only those displacement spectra whose large majority
322 (~80%) of spectral amplitudes are 3 times larger than the noise level in the
323 considered frequency band, assigning a lower weight to the part of the
324 spectrum with low S/N in the inversion process. As for the noise, according
325 to Abercrombie (1995) and Zollo et al. (2014), we have considered the pre-
326 P noise in a time-window whose length is equal to the selected signal
327 window length.
328 Both for P- and S-wave we have inverted the displacement spectra for
329 estimating the long-period spectral level spectral Ω_0 . We used a ω^{-2}
330 displacement source model (i.e., ζ= 2 and n = 1 in eq.4) and have inverted
331 also for attenuation parameters (Q_0). Note that, if the attenuation model is
332 known or a reasonable assumption can be made for the study area, it can be
333 fixed and only the source spectrum is inverted.
334 Finally, following Abercrombie (1995), both for P- and S-wave the final
335 value of Ω_0 is given by the vector composition of the single values
336 determined on each component, that is

$$\Omega_0 = \sqrt{\Omega_{0z}^2 + \Omega_{0NS}^2 + \Omega_{0EW}^2} \qquad (12)$$

The ratio of Ω_o^P to Ω_o^S values as function of the station azimuth and take-off angle (obtained from event location) thus represents the input data vector $\boldsymbol{d}^L$ for the Bayesian inversion described in the previous section. For all the analyzed earthquakes the model parameter space *M* is sampled at 2° step.

Events are located by using the manual P- and S-picks and a proper 1D velocity model. The P-polarities are used to obtain an independent estimate of the focal mechanism by using the FPFIT code (Reasenberg and Oppenheimer, 1985). Specifically, for the 23 December 2013, M_W 5.01, Matese earthquake we used the model proposed by Scognamiglio et al. (2009), for the synthetic test and for the 27 May 2009, M_L 2.9, Laviano earthquake the 1D velocity model proposed by Matrullo et al. (2013), and for the 27 September 2012, M_L 4.1, Benevento earthquake the model by Del Pezzo et al. (1983). Figure 2 displays the location of the events and the corresponding recording stations.

Results

The 23 December 2013, M_W 5.0, Matese earthquake

From late 2013 to early 2014 a sequence of about 250 events occurred in the Matese Massif that is a part of the Southern Apennines (Italy). Almost all the events occurred at 10-20 km depth (http://cnt.rm.ingv.it, last accessed 30

July 2015). The 23 December 2013, M_W 5.0, Matese earthquake represents the mainshock of the sequence. It occurred at a depth of about 20 km and is the largest event analyzed in the present study. As reported by INGV, the event was characterized by normal focal mechanism (ϕ = 324°, δ = 50° and λ = -78° (http://cnt.rm.ingv.it/tdmt/, last accessed 30 July 2015); see Figure 3) oriented NW-SE, parallel to the Apennine chain axis and represents our reference model.

The Matese earthquake has been recorded at 38 stations belonging to RAN and Italian Seismic Network. After a selection based on the spectral fit quality the number of available spectral ratios is reduced to 25, with epicentral distances ranging between 7 - 60 km (Figure 2a). Figure 4 shows the observed polarities and spectral ratio levels.

The retrieved MAP model for the Matese event is ϕ = 358°, δ = 46° and λ = -66° (ϕ = 145°, δ = 49° and λ = -112°) (Figure 3) that is in agreement with the model reported by INGV. The MAP model is plotted using a lower-hemisphere stereographic projection in Figure 4a together with the observed P-polarities. Figure 4b displays the comparison between observed and predicted $|\mathcal{R}^P|/|\mathcal{R}^S|$ ratios. The 68%, 90% and 95% Bayesian confidence intervals together with the 1D posterior marginal PDFs are shown in Figure 5. The slices representation of the *a-posteriori* pdf is shown in Figure S3 (available in the electronic supplement to this article) and indicates that the inferred solution is very well constrained. Note that, due to the azimuthal

distribution of the stations on the focal sphere the dip angle is highly constrained.

Synthetic test

Since, for small magnitude earthquakes the low signal-to-noise ratio generally prevents to have a high density of data and a good azimuthal coverage, we performed a synthetic test to evaluate the applicability of the technique to such earthquakes.

The synthetic waveforms were computed reproducing the features of the 27 May 2009, M_L 2.9, Laviano earthquake. We set the depth of the event at 13.5 km, seismic moment Mo = 2.8×10^{13} Nm, and strike, dip and rake to 280°, 40°, -100° (see Figure 3 for the beach ball representation). We generated synthetic seismograms using Axitra code (Cotton and Coutant, 1997) based on the discrete wavenumber approach for 1D layered model. We selected a triangle source-time function with 0.1s duration according to results of Stabile et al. (2012). The maximum simulated frequency was 50 Hz. We used the 1D velocity model proposed by Matrullo et al. (2013), a sampling rate of 0.005 s and a stations configuration reproducing the ISNet seismic network (Figure 2b). The epicentral distances cover a range of 8 - 47 km. Synthetics were manually picked (both P and S arrival times and P-wave polarities were identified) and the time-windows enclosing P- and S-waves arrival times were also manually selected. The windowed time-series were processed according to the procedure described in the Data analysis section. Figure 6b shows the observed $|\mathcal{R}^P|/|\mathcal{R}^S|$ ratios as function of the

station azimuth together with the same values obtained for the reference focal mechanism.

In order to test the Bayesian inversion procedure we used three different data sets: (a) $|\mathcal{R}^P|/|\mathcal{R}^S|$ ratios and polarities, (b) $|\mathcal{R}^P|/|\mathcal{R}^S|$ ratios, (c) all the $|\mathcal{R}^P|/|\mathcal{R}^S|$ ratios and only 8 polarities, respectively (for this latter condition standard codes based only on the polarities generally provide unconstrained solutions).

The obtained results indicate that, when both all the $|\mathcal{R}^P|/|\mathcal{R}^S|$ ratios and all the polarities are used, the Bayesian approach identifies the MAP model: ϕ = 274°, δ = 40° and λ = -112° that is well consistent with the values assumed for the simulations. The $|\mathcal{R}^P|/|\mathcal{R}^S|$ ratios corresponding to the MAP model together with the stereographic projection of the solution are shown in Figure 6a. The 68%, 90% and 95% Bayesian confidence intervals together with the 1D posterior marginal PDFs are shown in Figure 7a. In addition, the slices representation of the *a-posteriori* pdf at different dip values shows only two areas with probability different from zero (Figure S4, available in the electronic supplement to this article). Overall, these results indicate that the implemented procedure is able to accurately constrain both the principal and the auxiliary nodal plane

When only the $|\mathcal{R}^P|/|\mathcal{R}^S|$ ratios are inverted, since P-polarity data are not used, there is an intrinsic ambiguity (i.e., the sign of λ cannot be solved) that leads to identify as MAP models two solutions ϕ = 274°, δ = 40° and λ = ±112° with equal probability and produce large Bayesian confidence

intervals together with broad 1D posterior marginal PDFs (Figure 7b). Moreover, in this case the *a-posteriori* pdf, in addition to the MAP models, shows a number of secondary maxima (Figures 7b and S5, available in the electronic supplement to this article).

Generally, for small earthquakes the number of available P-polarities is small and the inferred solution might be highly uncertain. As an example, for the event simulated in this study, the solution obtained using only 8 P-polarities (Figure 2b) and FPFIT code is ϕ = 260°, δ = 58° and λ = -130°, which significantly differs from the reference model featuring a strike-slip component. However if these polarities are jointly inverted with the $|\mathcal{R}^P|/|\mathcal{R}^S|$ ratios in the Bayesian approach, the solution is expected to be improved. Indeed, the usage of all the $|\mathcal{R}^P|/|\mathcal{R}^S|$ ratios and only 8 polarities over the 21 available provides as MAP model: ϕ = 274°, δ = 40° and λ = -112° fitting the reference model but with slightly larger Bayesian confidence intervals (Figure 7c) compared to those obtained when all data are used (Figure 7a). The slices representation of the *a-posteriori* pdf at different dip values is shown in Figure S6, available in the electronic supplement to this article.

Figure 3 summarizes as case a, case b, and case c the inferred focal mechanisms together with their beach ball representation.

The 27 May 2009, M_L 2.9, Laviano earthquake

449 As regards the Laviano earthquake we have analyzed waveforms recorded at
450 15 stations of the ISNet network with epicentral distances between 8 - 46
451 km (Figure 2c).

452 We compared our solution with the model determined by Stabile et al.
453 (2012) from the analysis of 26 P-wave polarities identified on waveforms
454 recorded at both INGV and ISNet stations. The model is given by ϕ = 287°,
455 δ = 38° and λ = -102° (Figure 3). Note that, for the present study the
456 waveform for the stations AND3, BEL3, AVG3 and PGN3 of ISNet were
457 not available. However, in order to be consistent with synthetic test we
458 added in our inversion the polarities provided by Stabile et al. (2012).

459 The technique proposed in the present study identifies both the principal and
460 the auxiliary planes and, in particular, the MAP model corresponds to ϕ =
461 294°, δ = 40° and λ = -100° (Figure 3) that agrees with the model proposed
462 by Stabile et al. (2012). Thus a reduced number of P-polarities with respect
463 to that used by Stabile et al. (2012), but jointly inverted with the
464 $|\mathcal{R}^P|/|\mathcal{R}^S|$,ratios, allowed constraining the focal mechanism. The MAP
465 model is coherent with the expected focal mechanism of the earthquakes
466 occurring in the southern Apennines. In fact, being this portion of the
467 Apennines undergoing to an extensional regime, the larger portion of the
468 events feature a normal focal mechanism (Matrullo et al., 2013). Figure 8b
469 also shows the comparison between the observed $|\mathcal{R}^P|/|\mathcal{R}^S|$ ratios and
470 those corresponding to the MAP model and to the model by Stabile et al.
471 (2012), together with the P-polarities (Fig. 8a). The Bayesian confidence

intervals and marginal PDFs are shown in Figure 9. Notably, the slices representation of the *a-posteriori* pdf displays only two small areas of high pdf values in correspondence of the two nodal planes, indicating that the solution is very tightly constrained (Figure S7, available in the electronic supplement to this article).

The 27 September 2012, M_L 4.1, Benevento earthquake

The Benevento earthquake occurred in the northernmost part of the southern Apennines. Due to a transpressive stress regime acting in the area, focal mechanisms are characterized by a pronounced strike-slip component. This is the case of the 1930 event (Pino et al., 2008) and of two events occurred in 1962 (Westaway, 1987).

Waveforms available for Benevento earthquake have been recorded by ISNet, RAN and Rete Sismica Nazionale. Starting from an initial number of waveforms recorded at 16 stations, due to the quality of the recordings and the spectral fit, the number of spectral ratios reduced to 10 (Figure 2d) with epicentral distances ranging between 10 and 50 km, whereas the number of clearly identifiable P-wave polarities was 7. As a consequence this event represents an optimal case study to evaluate the performance of the proposed technique. In fact, while the number of polarities may be insufficient for using standard codes, their integration with a distribution of spectral ratios and a joint inversion can help to constrain the focal mechanism. In addition, focal mechanism for the Benevento earthquake has

been determined by other authors by using codes based on P-wave polarities inversion and from moment tensor inversion. In particular, Adinolfi et al. (2015) have found a strike slip focal mechanism with angles ϕ = 267°, δ = 75° and λ = 179° (indicated as Ref a in Figure 3). The Time Domain Moment Tensor (TDMT) technique implemented by the INGV (http://cnt.rm.ingv.it/tdmt, last accessed 30 July 2015) provided a focal mechanism with angles ϕ = 267°, δ = 68° and λ = -153° (indicated as Ref b in Figure 3). For the same event, using the ISOLA code (Sokos and Zahradník, 2008) and waveforms recorded at 14 stations belonging to ISNet, Michele et al. (2014) have determined a normal focal mechanism with a strong strike-slip component whose angles are ϕ = 246°, δ = 76° and λ = -143° (indicated as Ref c in Figure 3). Using the technique proposed in the present study we obtained the solutions: ϕ = 358°, δ = 52°, λ = -2° and ϕ = 89°, δ = 88°, λ= -142°. Figure 10a shows the stereographic projection corresponding to the MAP model together with P-polarities. The observed $|\mathcal{R}^P|/|\mathcal{R}^S|$ ratios, those corresponding to the MAP model and to the reference model are shown in Figure 10b.

The slices representation of the a-posteriori pdf shown in Figure S8 (available in the electronic supplement to this article) indicates that the *a-posterior* PDF is almost zero everywhere except in correspondence of the MAP model. However, looking at the Bayesian confidence intervals and marginal PDFs (Figure 11) it can be noted that the dip is characterized by the largest uncertainty.

In order to further test our code, we have inverted only for the spectral ratios by excluding the polarities. Aside from the ambiguity on the sign of the rake angle, the obtained mechanism (not shown here) is identical to the one determined from the joint inversion. Thus, we concluded that for the specific stations configuration relative to the Benevento earthquakes, the polarities have a minor effect on the final result with respect to the distribution of the observed spectral ratios.

Discussion and conclusion

In this study we have presented a technique that jointly inverts long-period spectral levels and P-wave polarities to infer focal mechanism in a Bayesian framework. Since the long-period spectral levels are observables usually available for both small and moderate-to-large earthquakes, this method can be used in a broader magnitude range compared to those operating only on small magnitude or only on moderate-large magnitude. The Bayesian approach offers the possibility to inherently consider additional observables as the S-polarization or P and S wave amplitudes. Moreover, it allows for a fully description of the inverted parameters through an *a-posteriori* pdf that permits to evaluate both the parameters uncertainty and correlation. This is very important for inverse problems where the relation between data and parameters is strongly non-linear as for the case of the focal mechanism. In this study, we computed the 68%, 90% and 95% Bayesian confidence intervals, the 1D *a-posterior* marginal PDFs and a slices representation of the *a-posteriori* pdf. All these analyses of the *a-posteriori* pdf provide information about the uncertainty of the inferred solution enlightening

possible secondary maxima and correlation among the parameters. However, the presence of at least two solutions is inherent to the assumed double-couple source model, which prescribes two equivalent nodal planes.

We tested the technique on events with different magnitude values, different focal mechanisms, and different network configuration (i.e., different number of stations, azimuthal gaps, …).

As an example of moderate normal-fault earthquake, we considered the 23 December 2013, M_W 5.0, Matese earthquake. For this event, the obtained solution is fully consistent with that obtained by INGV using TDMT inversion that can be more onerous in terms of required information and computational time.

For small earthquakes, large azimuthal gap of the recording stations, a poor signal-to-noise ratio and the related difficulty of correctly identifying first arrival phase and its polarity, may hamper the determination of the focal mechanism. Thus, before applying it to real earthquakes, we used synthetic events to simulate different network geometries and a different combination of long-period spectral ratios and P-polarities. As examples of real small magnitude earthquakes, we analyzed the 27 May 2009, M_L 2.9, Laviano earthquake and the 27 September 2012, M_L 4.1, Benevento earthquake that have different focal mechanism and different azimuthal coverage. The results suggest that for all the analyzed events, the addition of the spectral ratios also when a limited number of polarities are available, allows to

564 obtain a solution that well agrees with the solution obtained by other authors
565 with different techniques.

566 The results suggest that the approach is promising and could be applied in
567 those situations where the focal mechanisms of small magnitude
568 earthquakes may help to understand the stress regime and deformation
569 processes acting in an area. Moreover, since the long-period spectral levels
570 and P-polarities can be automatically measured, BISTROP could be
571 implemented for real-time applications. In the latter case, the selection of a
572 proper time window enclosing P- or S-wave is a key aspect, which may
573 require a preliminary calibration on a set of earthquakes of different
574 magnitude and location.

575

576 **Data & Resources**

577 Seismograms used in this study were obtained from: ISNet Data
578 Management Center at www.isnet.infn.it (last accessed November
579 2015); from the Italian Seismological Instrumental and Parametric
580 Data-Base (ISIDE) available at
581 http://iside.rm.ingv.it/iside/standard/index.jsp (last accessed
582 November 2015); from Italian acelerometric network (RAN) at
583 www.protezionecivile.gov.it (last accessed November 2015).

584 Figures have been generated with the Generic Mapping Tools (GMT,
585 Wessel and Smith, 1991).

The BISTROP code can be required contacting the corresponding author.

Acknowledgments

The authors thank the associated editor and three anonymous reviewers for their comments that helped to improve the manuscript.

References

Abercrombie, R. E. (1995). Earthquake source scaling relationships from −1 to 5 ML using seismograms recorded at 2.5 km depth, *J. Geophys. Res.* **100**, 24,015–24,036.

Adinolfi, G. M., R. De Matteis, A. Orefice, A. Zollo, R. De Nardis, R., and G. Lavecchia (2015). The September 27, 2012, ML 4.1, Benevento earthquake: A case of strike-slip faulting in Southern Apennines (Italy), *Tectonophysics*, **660**, 35-46, doi.org/10.1016/j.tecto.2015.06.036.

Aki, K., and P. G. Richards (1980). Quantitative Seismology, Theory and Methods, W.H. Freeman, San Francisco.

Aster, R. C., B. Borchers, and C. H. Thurber (2013). Parameter estimation and Inverse Problems, second edition, Elsevier, Amsterdam, 360 pp.

Ben-Menahem, A., and S. J. Singh (1981). Seismic Waves and Sources, 1108 p, Springer-Verlag, New York.

607 Boatwright, J. (1980). A spectral theory for circular seismic sources; simple
608 estimates of source dimension, dynamic stress drop, and radiated
609 seismic energy, *Bull. Seismol. Soc. Am*., **70** (7), 1–27.
610 Brillinger, D. R., A. Udías, and B. A. Bolt (1980). A probability model for
611 regional focal mechanism solutions, *Bull. Seism. Soc. Am.* **70**, 149-
612 170.
613 Carlin, P. B., and T. A. Louis (2009). Bayesian Methods for Data Analysis,
614 Chapman and Hall/CRC Press, Boca Raton.
615 Cotton, F., and O. Coutant (1997). Dynamic stress variations due to shear
616 faults in a plane-layered medium, *Geophys. J. Int.* **128** (3), 676–688.
617 Delouis, B. (2014). FMNEAR: Determination of Focal Mechanism and
618 First Estimate of Rupture Directivity Using Near-Source Records and
619 a Linear Distribution of Point Sources, *Bull. Seismol. Soc. Am.* **104,** 3,
620 1479-1500.
621 Del Pezzo, E., G. Iannaccone, M. Martini, and R. Scarpa (1983). The 23
622 November 1980 southern Italy earthquake, *Bull. Seismol. Soc. Am.* **73**,
623 187–200.
624 Dreger, D. S. (2003). 85.11 TDMT_INV: time domain seismic moment
625 tensor inversion, *Int. Geophys*. **81**, 1627.
626 Dreger, D. S., and D. V. Helmberger (1993). Determination of source
627 parameters at regional distances with three-component sparse network
628 data, *J. Geophys. Res*. **98** 8107-8125.

629 Fojtíková, L., and J. Zahradník (2014). A new strategy for weak events in
630 sparse network: The first-motion polarity solutions constrained by
631 single-station waveform inversion, *Seism. Res. Lett.* **85**, Number 6.
632 Hardebeck, J., and M. Shearer (2003). Using S/P Amplitude Ratios to
633 Constrain the Focal Mechanisms of Small Earthquakes, *Bull. Seism.*
634 *Soc. Am.* **93**, 6, pp. 2434–2444, December 2003.
635 Julian, B. R., and G. R. Foulger (1996). Earthquake mechanisms from
636 linear-programming inversion of seismic-wave amplitude ratios, *Bull.*
637 *Seism. Soc. Am.* **86** (4), 972-980.
638 Kisslinger, C. (1980). Evaluation of S to P amplitude rations for
639 determining focal mechanisms from regional network observations,
640 *Bull. Seism. Soc. Am.* **70** (4), 999-1014.
641 Kisslinger, C., J. R. Bowman, and K. Koch (1981). Procedures for
642 computing focal mechanisms from local (SV/P) z data, *Bull. Seism.*
643 *Soc. Am.* **71** (6), 1719-1729.
644 Iannaccone, G., A. Zollo, R. De Matteis, and A. Deschamps (1994). Rupture
645 characterization of a low magnitude earthquake of central Apennines
646 (Italy), *Phys. Earth Plan. Int.* **82**, 157-165.
647 Imanishi, K., T. Uchide, and N. Takeda (2016). Determination of focal
648 mechanisms of nonvolcanic tremor using S wave polarization data
649 corrected for the effects of anisotropy, *Geophys. Res. Lett.* 43, 611–
650 619, doi:10.1002/2015GL067249.
651 Matrullo E., R. De Matteis, C. Satriano, O. Amoroso, and A. Zollo (2013).
652 An improved 1D seismic velocity model for seismological studies in

653 the Campania-Lucania region (Southern Italy), *Geophys. J. Int.* **195**,
654 Issue 1, pp.460-473, doi: 10.1093/gji/ggt224.
655 Michele, M., S. Custódio, and A. Emolo (2014). Moment tensor resolution:
656 case study of the Irpinia Seismic Network, Southern Italy, *Bull.*
657 *Seismol. Soc. Am.* **104**, 1348-1357, doi: 10.1785/0120130177.
658 Morozov, I. B. (2008). Geometrical attenuation, frequency dependence of
659 Q, and the absorption band problem, *Geophys, J. Int.* **172**, 239–252,
660 doi:10.1111/j.1365-246X.2008.03888.x.
661 Pino, N. A., B. Palombo, G. Ventura, B. Perniola, and G. Ferrari (2008).
662 Waveform modeling of historical seismograms of the 1930 Irpinia
663 earthquake provides insight on "blind" faulting in Southern Apennines
664 (Italy), *J. Geophys. Res.* **113**, no. B5, doi: 10.1029/2007JB005211.
665 Rau R. J., F. T. Wu, and T.C. Shin (1996). Regional network focal
666 mechanism determination using 3D velocity model and SH/P
667 amplitude ratio, *Bull. Seismol. Soc. Am.* **86** (5), 1270-1283.
668 Reasenberg, P. A., and D. Oppenheimer (1985). FPFIT, FPPLOT, and
669 FPPAGE:Fortran computer programs for calculating and displaying
670 earthquake fault-plane solutions, U.S. Geol. Surv. Open-File Rep. 85-
671 739.
672 Scognamiglio, L., E. Tinti, and A. Michelini (2009). Real-time
673 determination of seismic moment tensor for the Italian region, *Bull.*
674 *Seismol. Soc. Am.* **99** (4), 2223-2242.
675 Shen Y., D. W. Forsyth, J. Conder, and L. M. Dorman (1997). Investigation
676 of microearthquake activity following an intraplate teleseismic swarm

677 on the west flank of the southern East Pacific Rise, *J. Geophys. Res.*
678 **102** (B1), 459-475.
679 Snoke J. A. (2003). FOCMEC: focal mechanism determinations,
680 International Handbook of Earthquake and Engineering Seismology,
681 1629-1630.
682 Sokos, E. N., and J. Zahradník (2008). ISOLA a Fortran code and a Matlab
683 GUI to perform multiple-point source inversion of seismic data,
684 *Computers and Geosciences* **34**, 967-977.
685 Stabile T.A., C. Satriano, A. Orefice, G. Festa, and A. Zollo (2012).
686 Anatomy of a microearthquake sequence on an active normal fault,
687 *Sci. Rep*. **2**. doi:10.1038/srep00410.
688 Zahradník, J., J. Janskļý, and K. Papatsimpa (2001). Focal mechanisms of
689 weak earthquakes from amplitude spectra and polarities, *Pure and*
690 *applied geophysics*, **158**: 647-665. Birkhäuser Verlag, Basel.
691 Zollo, A., and P. Bernard (1991). Fault mechanism from near source data:
692 joint inversion of S polarizations and P polarities, *Geophys. J. Int.*
693 **104**, 441-451.
694 Zollo, A., A. Orefice, and V. Convertito (2014). Source Parameter Scaling
695 and Radiation Efficiency of Microearthquakes Along the Irpinia Fault
696 Zone in Southern Apennines, Italy, *J. Geophys. Res.* **119**, 4, 3256–
697 3275. DOI: 10.1002/2013JB010116.
698 Walsh, D. R. Arnold, and J. Townend (2009). A Bayesian approach to
699 determining and parametrizing earthquake focal mechanisms,

Geophys. J. Int. **176**, 235-255, DOI: 10.1111/j.1365-246X.2008.03979.x.

Weber, E., V. Convertito, G. Iannaccone, A. Zollo, A. Bobbio, L. Cantore, M. Corciulo, M. Di Crosta, L. Elia, C. Martino, A. Romeo, and C. Satriano (2007). An advanced seismic network in southern Apennines (Italy) for seismicity investigations and experimentation with earthquake early warning, *Seismol Res. Lett*. 78:622–634.

Wessel, P., and W. H. F. Smith (1991). Free software helps map and display data, *EOS Trans*. AGU, 72, 445–446.

Westaway, R. (1987). The Campania, southern Italy, earthquakes of 1962 August 21, *Geophys. J. Roy. Astron. Soc.* **88**, no. 1, 1–24, doi: 10.1111/j.1365-246X.1987.tb01366.x.

Figure Captions

Figure 1: a) Example of analysed waveforms together with the manually selected time windows enclosing P- and S-waves picking. b) left panel: displacement spectrum of the P-wave (grey line) computed on the selected window, the fitting curve (black line) and the pre-P noise displacement spectrum (dashed grey line); right panel: same as left panel but for a window length reduced by 30%. c) Same as panel b) but for S-wave.

Figure 2: Geographic distribution of seismic stations (triangle) and epicenter location (star) of the analyzed events. a) the 23 December 2013, M_W 5.0, Matese earthquake; b) M_L 2.9 synthetic earthquake; the black triangles identify the stations whose P polarities have been used in the test *c*

described in the paragraph "*Synthetic test";* c) the 27 May 2009, M_L 2.9, Laviano earthquake; d) the 27 September 2012, M_L 4.1, Benevento earthquake.

Figure 3: MAP models obtained from the BISTROP procedure for the analyzed events (black beach-balls). As for the synthetic event, the MAP models for the three tests are indicated as case a, case b and case c (see the text for details). For each event, the gray beach-balls represent the solutions by other authors obtained by using different data and techniques.

Figure 4: a) stereographic projection of the solution corresponding to the MAP model. P and T axes are identified by grey diamond and grey hexagon respectively. Black squares represent compression first motion while empty gray squares represent dilatational first motion. The symbol size is proportional to the observed $|\mathcal{R}^P|/|\mathcal{R}^S|$ ratios; b) observed $|\mathcal{R}^P|/|\mathcal{R}^S|$ ratios (black cross) as a function of stations azimuth compared with those predicted by using the MAP model (grey circle) and those predicted by using the model proposed by the authors indicated in the text and also reported in Figure 3 (black diamond).

Figure 5: Upper panels: 1-D marginal a-posterior pdfs on each inverted parameter. Lower panels: 68%, 90% and 95% Bayesian confidence intervals.

Figure 6: Same as Figure 4, but for the M_L 2.9 synthetic earthquake and case a (see the text for details).

Figure 7: a) Left panels: 68%, 90% and 95% Bayesian confidence intervals. Right panels: 1-D marginal a-posterior pdfs on each inverted parameter for

748 the test indicated as case a (see the text for details). b) same as a) but for the
749 test indicated as case b. c) same as a) but for the test indicated as case c.
750 **Figure 8**: Same as Figure 4, but for the 27 May 2009, M_L 2.9, Laviano
751 earthquake.
752 **Figure 9:** Same as Figure 5 but for the 27 May 2009, M_L 2.9, Laviano
753 earthquake.
754 **Figure 10**: Same as Figure 4, but for the 27 September 2012, M_L 4.1,
755 Benevento earthquake.
756 **Figure 11:** Same as Figure 5 but for the 27 September 2012, M_L 4.1,
757 Benevento earthquake.
758
759
760

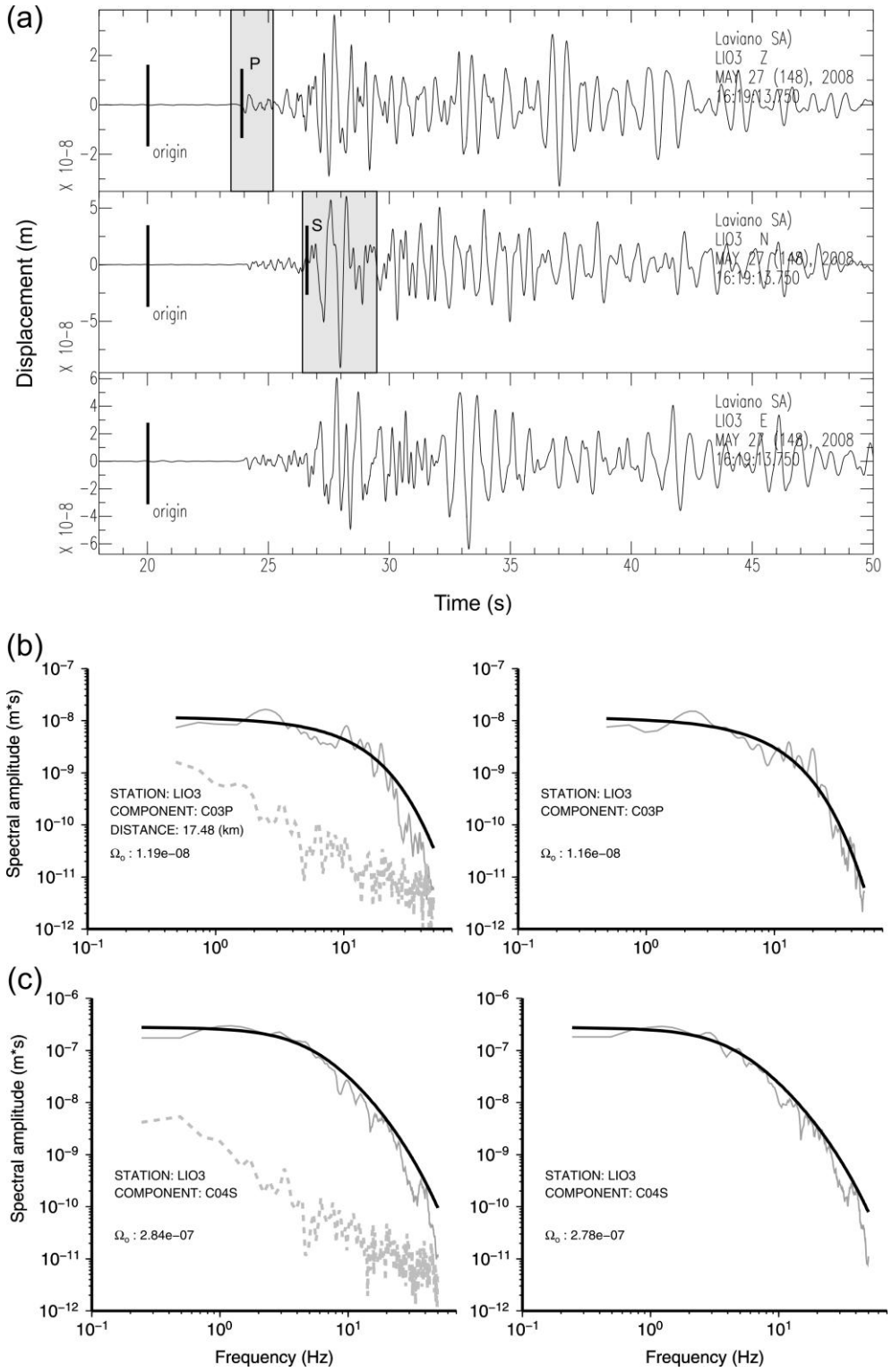
(a)
Laviano SA)
LIO3 Z
MAY 27 (148), 2008
16:19:13.750
P
origin
X 10-8
Laviano SA)
LIO3 N
MAY 27 (148), 2008
16:19:13.750
S
origin
X 10-8
Laviano SA)
LIO3 E
MAY 27 (148), 2008
16:19:13.750
origin
X 10-8
Displacement (m)
Time (s)
(b)
Spectral amplitude (m*s)
STATION: LIO3
COMPONENT: C03P
DISTANCE: 17.48 (km)
Ωo : 1.19e-08
STATION: LIO3
COMPONENT: C03P
Ωo : 1.16e-08
(c)
Spectral amplitude (m*s)
STATION: LIO3
COMPONENT: C04S
Ωo : 2.84e-07
STATION: LIO3
COMPONENT: C04S
Ωo : 2.78e-07
Frequency (Hz)
Frequency (Hz)

Figure 1

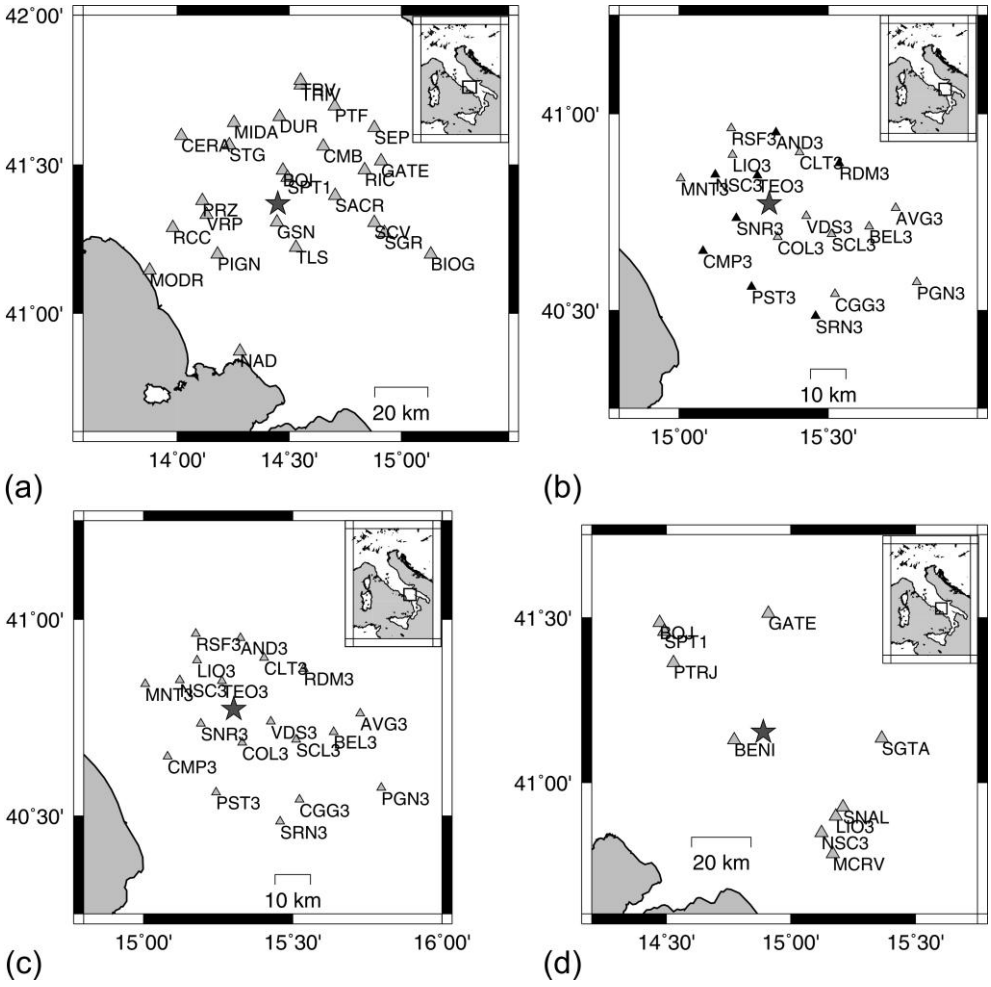
42°00'
41°30'
41°00'
14°00'
14°30'
15°00'
TRV
PTF
DUR
MIDA
SEP
CERA
STG
CMB
GATE
BOI
SPT1
RIC
SACR
RRZ
VRP
GSN
SCV
RCC
SGR
TLS
PIGN
BIOG
MODR
NAD
20 km
(a)
41°00'
40°30'
15°00'
15°30'
RSF3
AND3
LIO3
CLT3
RDM3
MNT3
NSC3
TEO3
AVG3
SNR3
VDS3
BEL3
COL3
SCL3
CMP3
PST3
CGG3
PGN3
SRN3
10 km
(b)
41°00'
40°30'
15°00'
15°30'
16°00'
RSF3
AND3
LIO3
CLT3
RDM3
MNT3
NSC3
TEO3
AVG3
SNR3
VDS3
BEL3
COL3
SCL3
CMP3
PST3
CGG3
PGN3
SRN3
10 km
(c)
41°30'
41°00'
14°30'
15°00'
15°30'
GATE
BOI
SPT1
PTRJ
BENI
SGTA
SNAL
LIO3
NSC3
MCRV
20 km
(d)

Figure 2

774

775

776

777

778

779 **Figure 3**

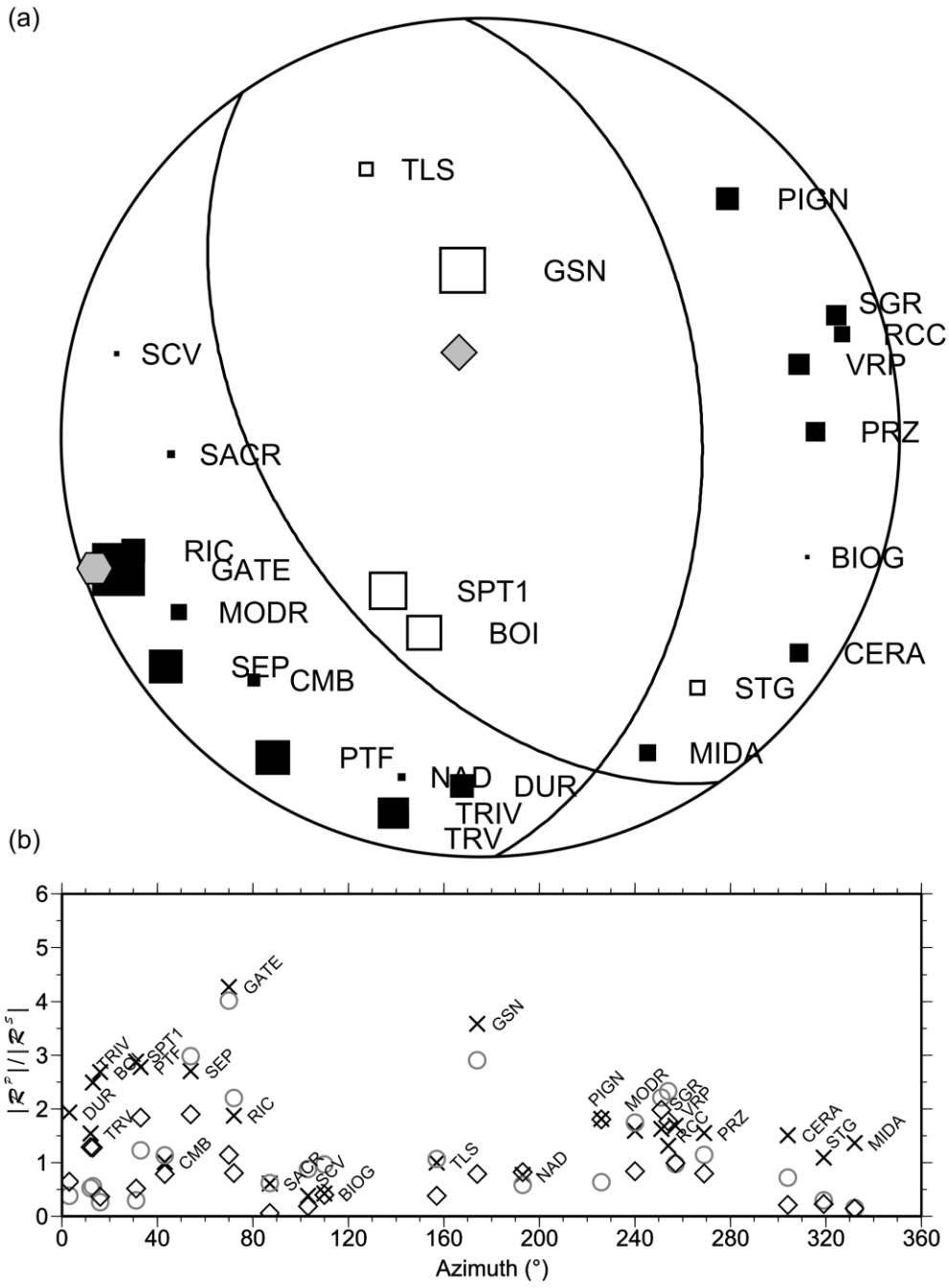
(a)
TLS
PIGN
GSN
SGR
RCC
SCV
VRP
PRZ
SACR
BIOG
RIC
GATE
SPT1
MODR
BOI
CERA
SEP
CMB
STG
PTF
MIDA
NAD
DUR
TRIV
TRV
(b)
Azimuth (°)

Figure 4

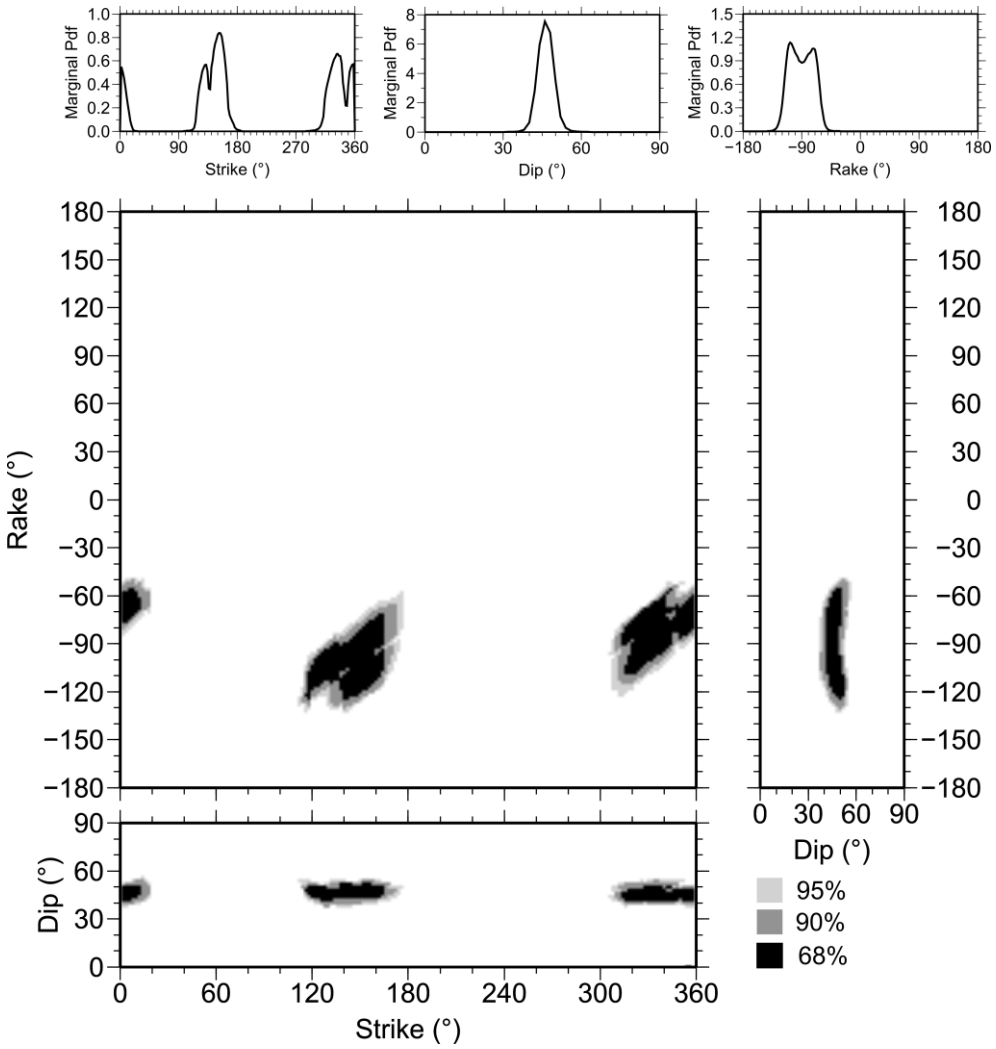

Figure 5

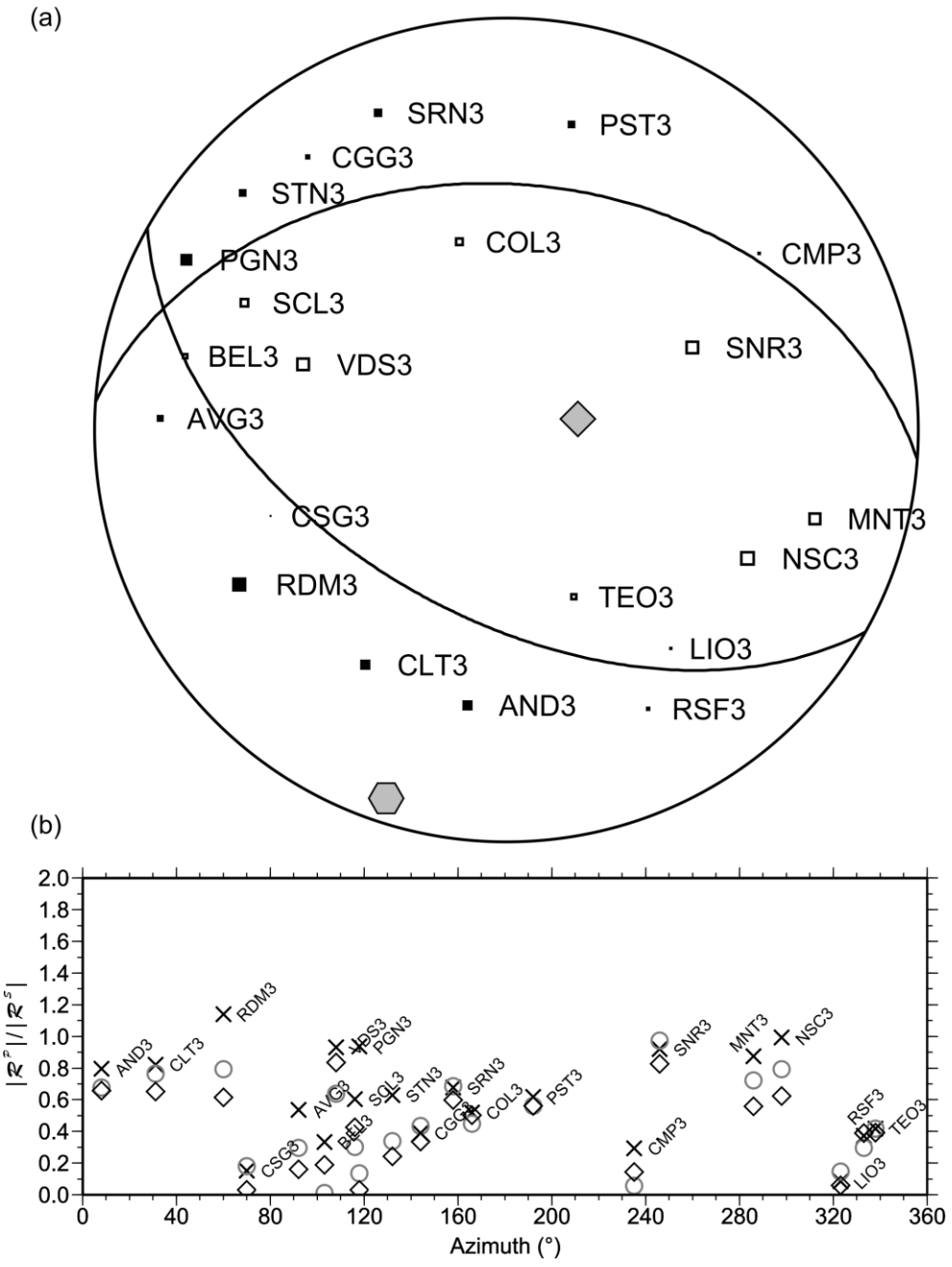
(a)
SRN3
PST3
CGG3
STN3
COL3
CMP3
PGN3
SCL3
SNR3
BEL3
VDS3
AVG3
CSG3
MNT3
NSC3
RDM3
TEO3
LIO3
CLT3
AND3
RSF3
(b)
2.0
1.8
1.6
1.4
1.2
1.0
0.8
0.6
0.4
0.2
0.0
0
40
80
120
160
200
240
280
320
360
Azimuth (°)

Figure 6

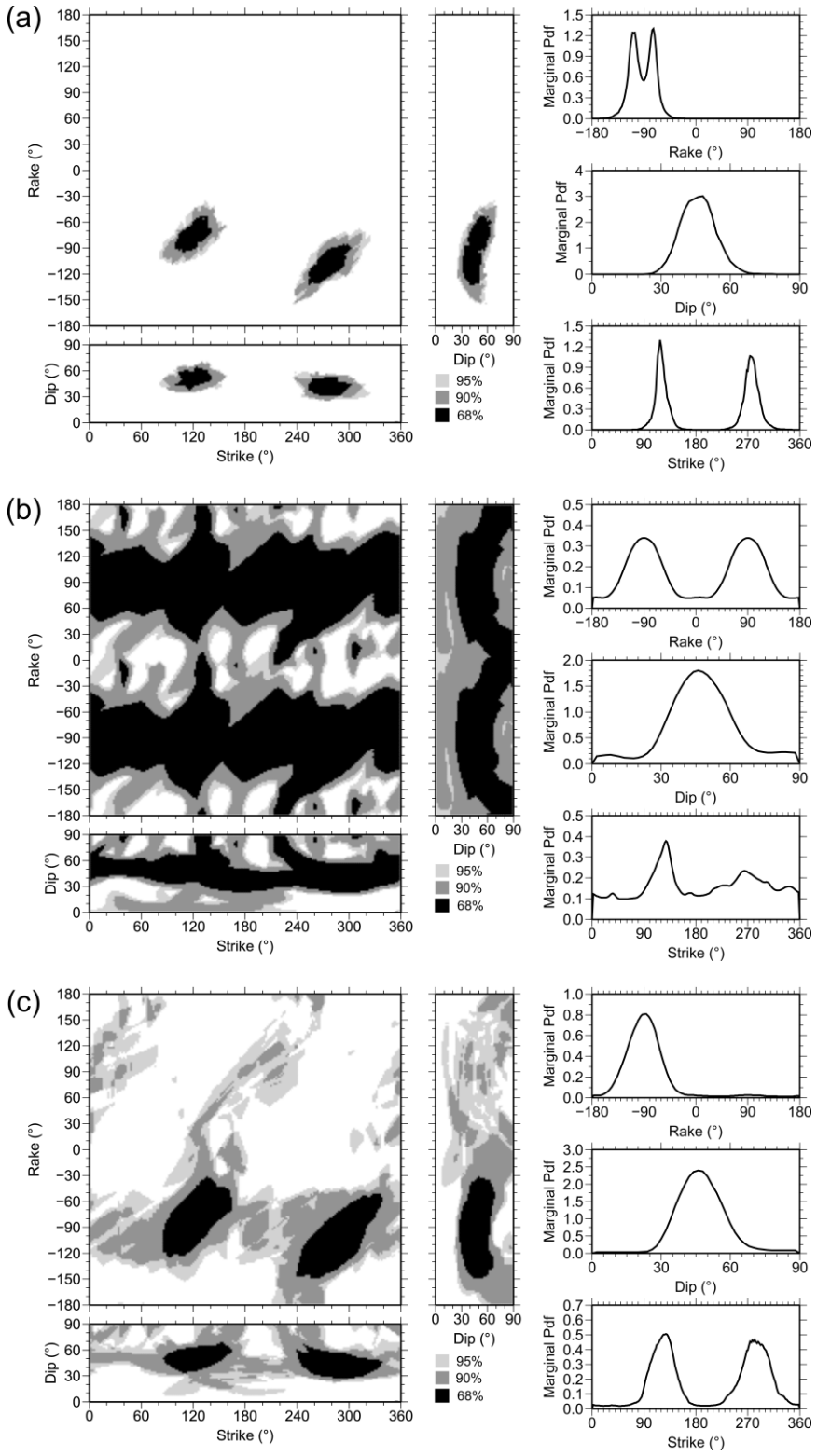

Figure 7

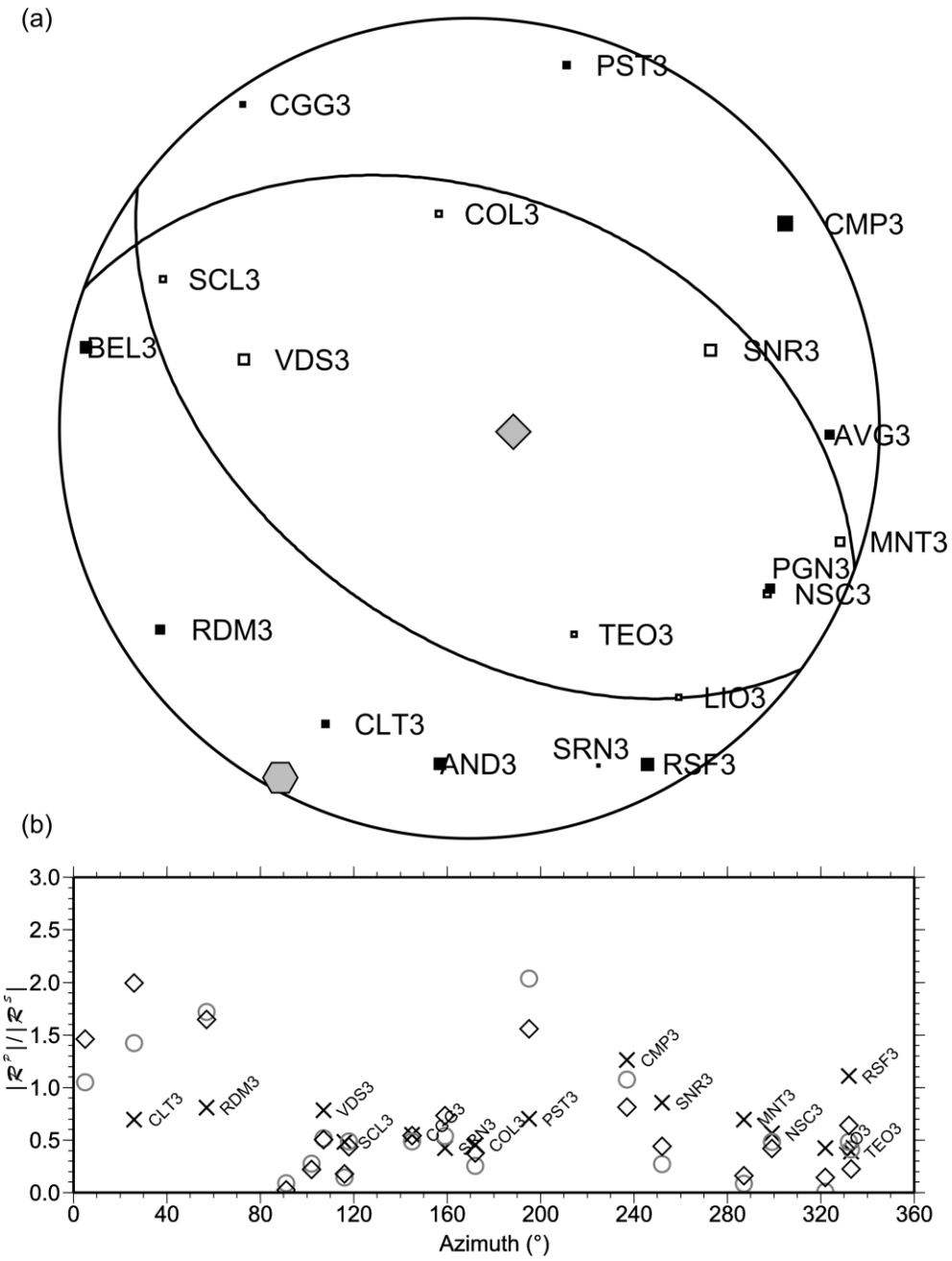
(a)
PST3
CGG3
COL3
CMP3
SCL3
BEL3
VDS3
SNR3
AVG3
MNT3
PGN3
NSC3
RDM3
TEO3
LIO3
CLT3
SRN3
AND3
RSF3
(b)
3.0
2.5
2.0
1.5
1.0
0.5
0.0
0
40
80
120
160
200
240
280
320
360
Azimuth (°)
CLT3
RDM3
VDS3
SCL3
CGG3
SRN3
COL3
PST3
CMP3
SNR3
MNT3
NSC3
RSF3
TEO3

Figure 8

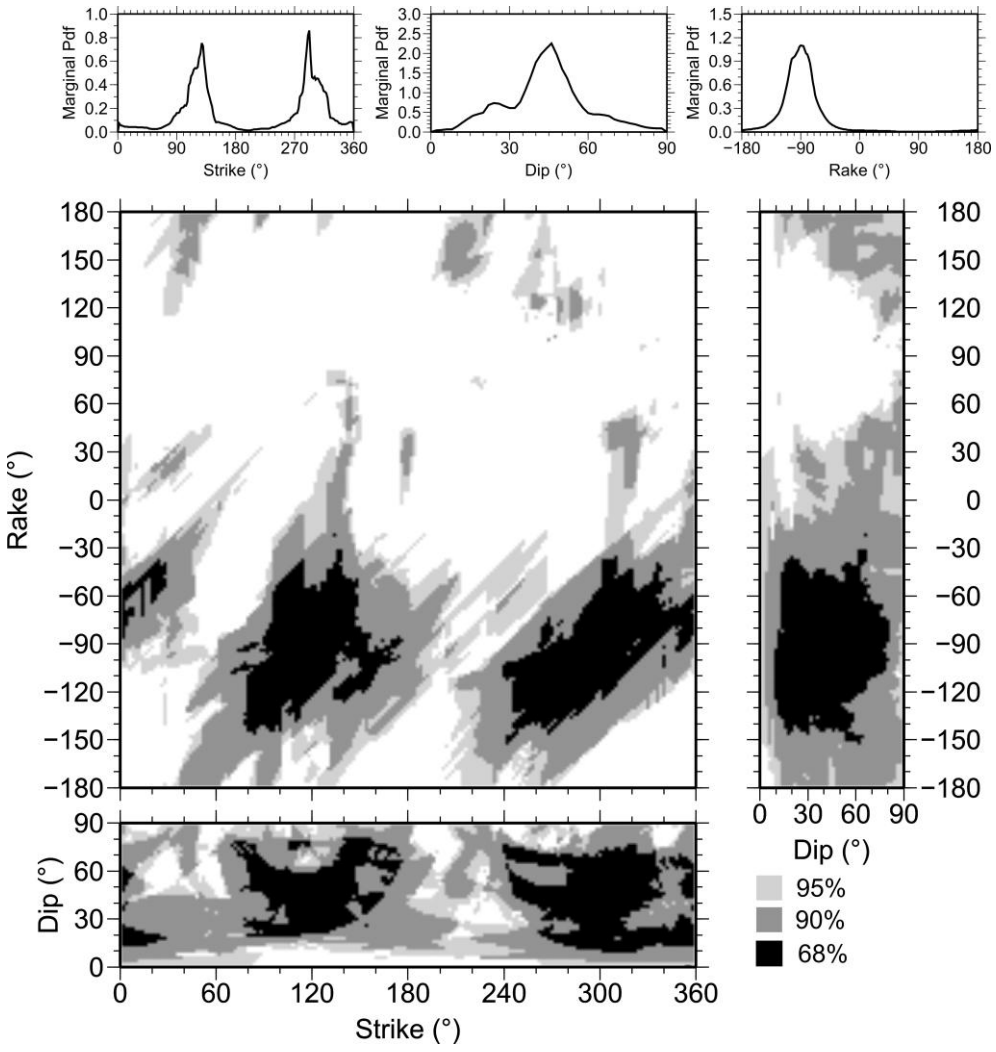

Figure 9

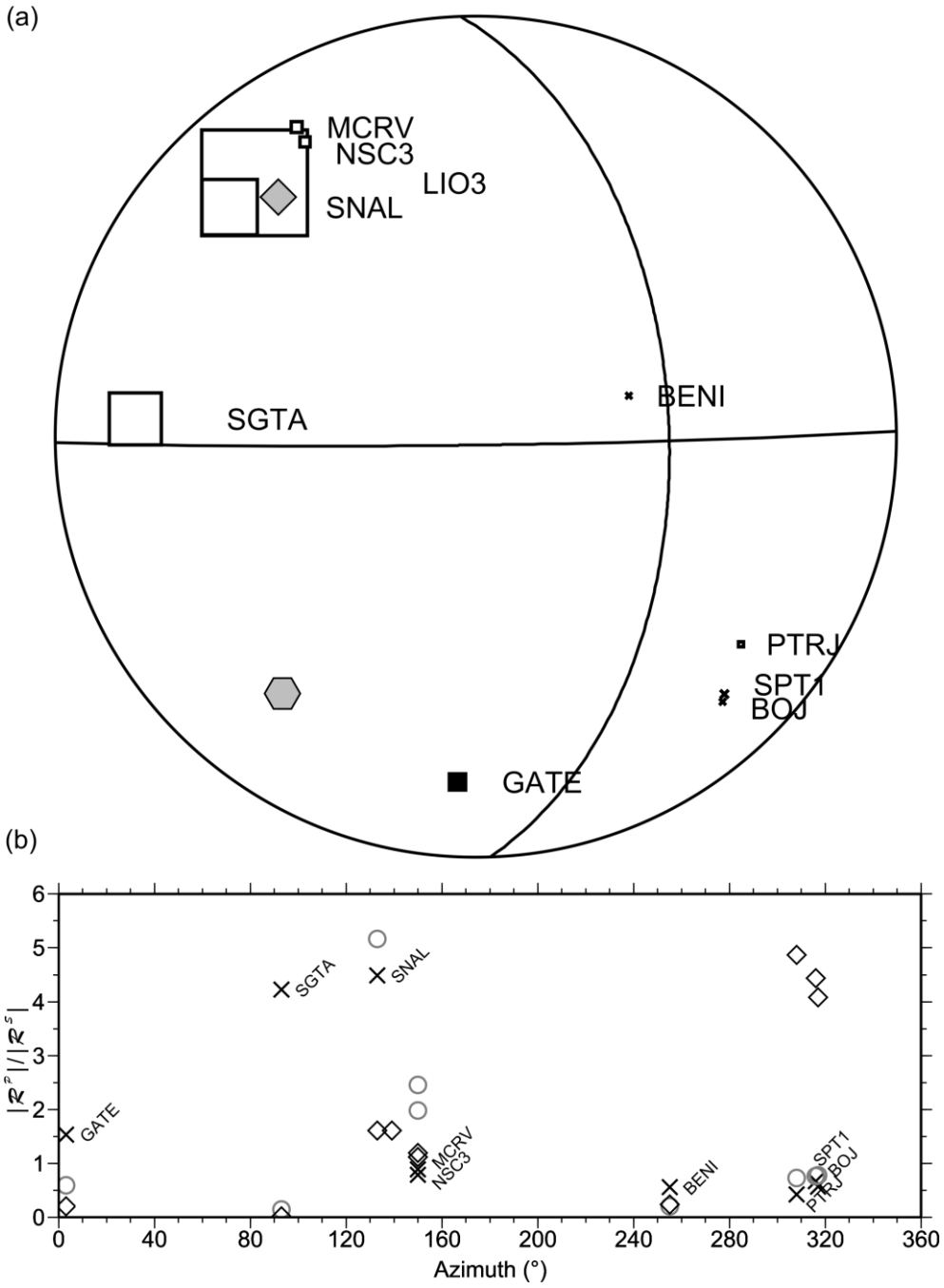
(a)
MCRV
NSC3
LIO3
SNAL
SGTA
BENI
PTRJ
SPT1
BOJ
GATE
(b)
|R^P|/|R^S|
Azimuth (°)
0
40
80
120
160
200
240
280
320
360
1
2
3
4
5
6
GATE
SGTA
SNAL
MCRV
NSC3
BENI
SPT1
PTRJ
BOJ

Figure 10

836

837

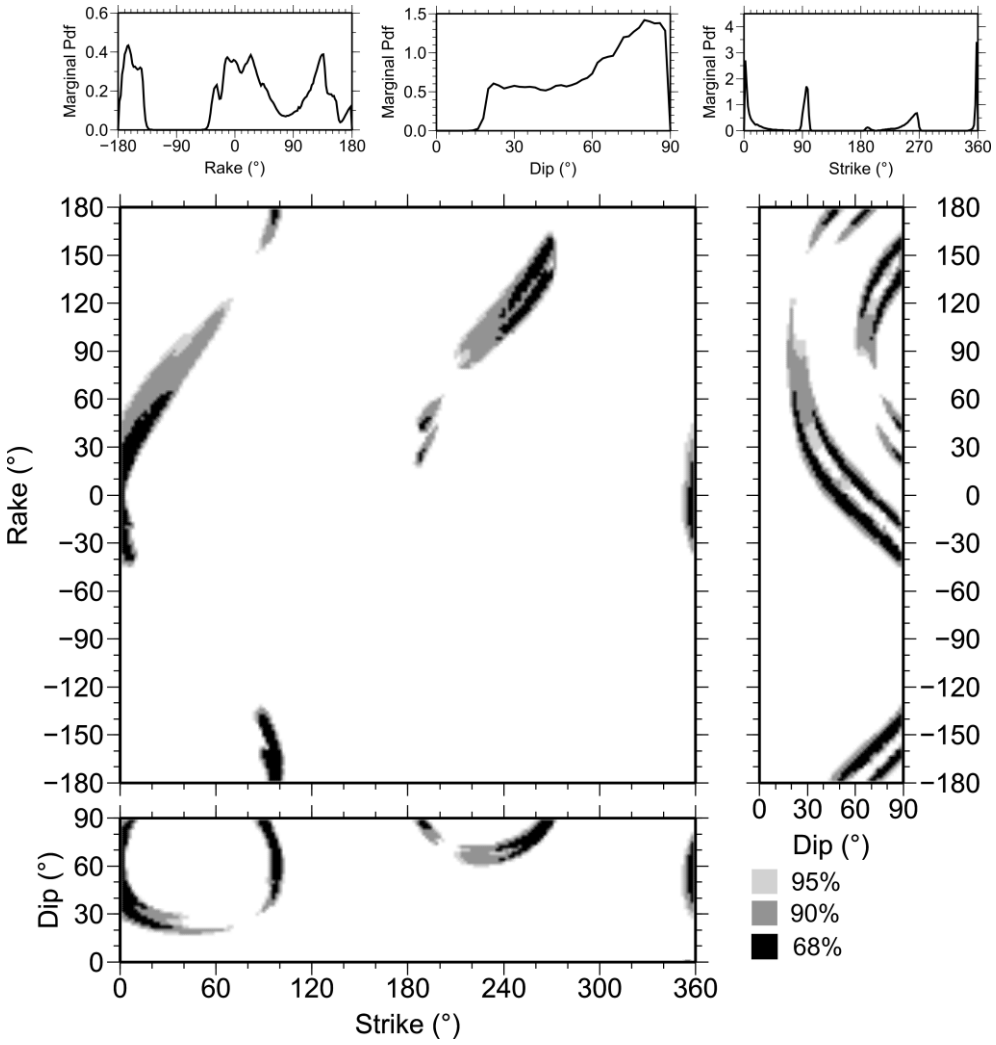

838

839

840 **Figure 11**

841

842